Hematite coated, conductive Y doped ZnO nanorods for high efficiency solar water splitting

Article (Accepted Version)

Hematite coated, conductive Y doped ZnO nanorods for high efficiency solar water splitting

To cite this article before publication: Daniel Commandeur *et al* 2020 *Nanotechnology* in press https://doi.org/10.1088/1361-6528/ab776c

Hematite Coated, Conductive Y doped ZnO Nanorods for High Efficiency Solar Water Splitting

Daniel Commandeur, Joshua McGuckin and Qiao Chen*

Department of Chemistry, School of Life Sciences, University of Sussex, Brighton, BN1 9QJ, UK

*Corresponding Author, Email to: qiao.chen@sussex.ac.uk

Abstract

For the first time, hematite (α-Fe_2O_3) crystals were electrochemically deposited over vertically aligned conductive zinc oxide nanorods (NR) to form a specially designed 3D heterostructure with a unique triple layer structure. The structure formed with a thin layer of $ZnFe_2O_4$ sandwiched between the hematite and the ZnO, which forms a barrier to reduce the back migration of holes. Hence, the charge separation is significantly improved. The small unequal band gaps of α-Fe_2O_3 and $ZnFe_2O_4$ help to enhance and broaden visible light absorption. The electron transportation was further improved by yttrium doping in the ZnO (YZnO) NRs, resulting in increased conductivity. This allowed the vertically aligned NRs to perform as electron highways, which also behave as effective optical waveguides for improved light trapping and absorption, since ZnO absorbs little visible light. All these benefits made the unique structures suitable for high performance photoelectrochemical (PEC) water splitting. Optimisation of α-Fe_2O_3 thickness led to a photocurrent density improvement from 0.66 to 0.95 mA cm^{-2} at 1.23 V_{RHE}. This was further improved to 1.59 mA cm^{-2} by annealing at 550°C for 3 hours, representing a record-breaking photocurrent for α-Fe_2O_3/ZnO systems. Finally IPCE confirmed the successful generation and transfer of photoelectrons under visible light

excitation in the specifically designed heterostructure photoanode, with 5% efficiency for blue light, and 15% for violet light.

Keywords: Y Doped ZnO Nanorods, Solar Water Splitting, Hematite Coating, Optical Waveguide

1 Introduction

Great innovation and radical new solutions are required to meet the threat posed by climate change.[1] Although great progress has been achieved in renewable energy generation, one of the key factors restricting electrification is energy storage.[2] PEC water splitting provides an elegant solution, harvesting and storing solar energy in chemical H_2 bonds.[3–5] Requiring aqueous insolubility and band edge positions suitable to surmount the over potentials for water redox, metal oxides such as TiO_2 and ZnO have been the focus of much literature for this application.[6–9] Boasting superior electronic properties and the simple solution growth of nanostructures, ZnO has yet to reach its full potential for solar water splitting.[10] The main restriction is its large band gap, 3.2 eV, rendering this material unable to absorb most sunlight, although this factor can be negated through the use of doping and coating.[11]

This has led to the investigation of many small band gap semiconductors for visible light sensitisation, including CdS,[12] MoS_2,[13] WO_3,[14] Ta_3N_5,[15] $BiVO_4$,[16] g-C_3N_4[17] and α-Fe_2O_3.[18] Hematite (α-Fe_2O_3) is an excellent candidate to facilitate the photocatalytic water splitting reaction. It absorbs a greater portion of the solar spectrum with a narrow band gap of 2.1 eV. However, it suffers from poor charge transportation. The room temperature charge mobility for hematite is of the order of 10^{-2} $cm^2/V{\cdot}s$,[19,20] compared to 166 $cm^2/V{\cdot}s$ for ZnO NRs.[21] Hence, its diffusion length of minor charge carriers (holes) is extremely short (2–4 nm) and so is the lifetime of charge carriers (6 ps, ~1000 times shorter than TiO_2), resulting in the high probability of electron–hole recombination.[22–24] Meanwhile, hematite also has a relatively low optical absorption coefficient, due to its indirect band gap.[25] A minimum film thickness of 400 nm is needed to absorb 95% of the light at 550 nm.[26]

In fact, limited charge mobility and high recombination rate are the common problems for many semiconductors due to partial hybridisation of electronic structures. For hematite, several approaches have been taken to overcome the mobility problem. Firstly, dopants were introduced to modify various aspects of hematite properties selectively.[25] Adding tetravalent cations, such as Si^{4+} and Ti^{4+}, has helped achieve the highest photocatalytic water splitting performances so far.[27,28] Alternatively, innovations in the design of morphologies also show promise. For example nanostructured hematite, like NRs,[29] nanowires,[30] cauliflowers,[31] or highly porous films could also address poor minority carrier diffusion.[32] With specific anisotropic nanoscale morphologies, charge recombination can be effectively reduced, resulting in significantly improved photocatalytic performance.[33] However, such unsupported nanostructures with material thickness of 4-5 nm could significantly weaken the mechanical and chemical stability of hematite. Hence, a new composite nanostructure design has been developed to achieve both improved charge mobility as well as short charge diffusion pathways, without sacrificing the stability of the hematite materials. For example, hematite nanocrystals were deposited on conductive nanowires made of Au and Si,[34,35] obtaining structures with conductive cores and hematite shells. However, due to the opaque nature of Au and Si, the light scattering within the nanostructures and light absorption by hematite is highly restricted. This in turn, could limit the photocatalytic performance.[34]

Although doping tetravalent cations can improve the overall photocatalytic performance, the approach is specifically effective for hematite.[27,28] Hence, it is important to develop a universal design that can be applied to any photocatalyst suffering from limited charge mobility and weak light absorption. In this paper, we present a 3D electrode platform based on vertically

aligned transparent conductive oxide (TCO) nanorods. The TCO structure is formed with YZnO nanorods (NR) synthesised by rapid microwave assisted chemical deposition.[36] Hematite nanocrystals were deposited on the TCO NRs to test the enhancement of photocatalytic water splitting performance. In our previous work, Y doping has shown favourable effects due to high conductivity and increased NR aspect ratio.[37] The high conductance of the NRs minimises the energy cost with rapid photoelectron transport.[37] ZnO is transparent in the visible light region, hence the vertically aligned NRs behave as optical waveguides for visible light. The photonic advantages are made clear in Fig. S1, where simple Fresnel calculations show total internal reflectance above 40° of incident angle from ZnO to aqueous electrolyte. Conversely, light trapped within the ZnO has a finite probability of transmitting into the iron oxide at all incident angles, implying effective light trapping and delivery. With side-emitted light scattered between α-Fe_2O_3 thin films, light illumination and absorption can be significantly improved. As such, only a very thin layer of hematite (8~16 nm) was required to coat the YZnO NRs, allowing a short diffusion distance for minority charge carriers to the electrolyte. By combining α-Fe_2O_3 with TCO, YZnO NRs, the weaknesses of α-Fe_2O_3, including: Limited charge mobility; short hole diffusion length; poor light absorption and the mechanical stability of the nanostructured hematite can be effectively overcome. More importantly, this novel design can be generally applied to any semiconductor materials with similar weaknesses.

Furthermore, upon annealing of the sample at 550°C, a $ZnFe_2O_4$ layer was formed at the interface between YZnO and α-Fe_2O_3. This material has a favourable band structure with smaller band gap energy relative to YZnO and α-Fe_2O_3. Therefore, a wider range of solar spectrum can be harvested.

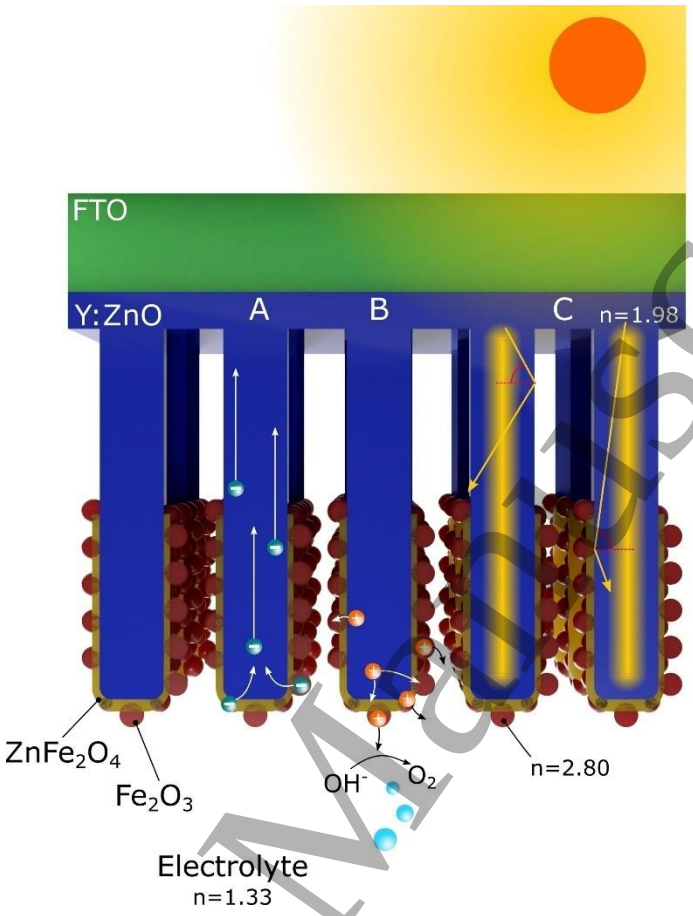

Figure 1: The YZnO/$ZnFe_2O_4$/Fe_2O_3 triple junction architecture of designed 3D photoanode with key mechanisms affecting the solar water splitting. The mechanisms include A, rapid electron transportation using conductive Y doped ZnO; B, short hole diffusion pathways to electrolyte and C, the visible light waveguiding through light scattering and side emission through ZnO NRs.

In this work we demonstrate the benefits of doping ZnO with yttrium, and the electrochemical deposition and formation of Fe_2O_3 nanoparticles, which increase effective surface area to facilitate rapid evolution of oxygen under visible light excitation. Furthermore, the triple junction of YZnO/$ZnFe_2O_4$/Fe_2O_3 structure allows efficient charge separation

evidenced by electrical impedance spectroscopy. The structure of the 3D photoanode design, light scattering and absorption, short hole diffusion pathways as well as fast charge transportation are summarised in Figure 1. Under optimised conditions, a top performance of 1.59 mA/cm^2 at 1.23 V_{RHE} was achieved, launching the novel nanostructured photoanodes to one of the highest performances in literature. The success of the junction is down to the suppression of electron hole recombination in the iron oxide species, alongside the effective electron transportation and light illumination through the TCO, YZnO NRs.

2 Experimental Methods

2.1 Y doped ZnO Synthesis

Transparent conducting glass substrates (fluorine doped tin oxide, FTO) of 12 × 20 mm^2 were cleaned by sonication in a sequence of acetone, isopropanol and DI water for 20 minutes each. The substrate was seeded using a 0.1 M zinc acetate solution in DI water with added 0.6 wt% polyvinyl alcohol for viscosity. The solution was spin coated using a two stage program, 800 RPM for 90 seconds followed by 30 seconds at 2000 RPM. This was followed by annealing in air at 500°C for 20 minutes to form the zinc oxide seeding layer.[38] The vertically aligned NRs were synthesised using a rapid microwave assisted deposition described in previous work.[36] Briefly, the substrate was placed face down in 20 ml aqueous solution of 40 mM zinc nitrate and hexamethyltetramine (HMT) in 1:1 molar ratio. The sample was heated at microwave power of 100 W to 100°C for a 30 minute holding time.[36] A total of 4 heating cycles were used for each sample. Samples were subsequently annealed in air at 500°C for 30 minutes. Yttrium doped samples were produced using 1% molar addition of yttrium nitrate (with respect to zinc nitrate) to the growth solution. The achieved dopant concentration was previously measured to be 0.10 at% by ICP-MS.[37]

2.2 Electrochemical deposition of Fe_2O_3

All chemicals were purchased from Sigma Aldrich without further purification. Layers of iron oxide of various thicknesses were formed on the surface of the YZnO NRs by electrochemical deposition. Firstly an aqueous solution of 0.1 mM $FeCl_3$ was prepared and transferred to a 100 ml round bottom flask. The YZnO NR on FTO glass sample and a counter electrode of stainless steel foil were inserted into the $FeCl_3$ solution. The sealed system was then sonicated under vacuum condition to draw out the air between the NRs, shown in Figure S2A. In order to control the deposition rate and film thickness, constant electrochemical potentials were applied at -1.08, -1.15, -1.56 and -1.89 V respectively, which offers steady deposition current density of 20, 40, 80 and 120 $\mu A/cm^2$. The typical transient current density behaviour is shown in Figure S2C. The deposition time was fixed for 1 hour for all samples. Therefore, the film quality and thickness is controlled by the deposition rate, which is reflected by the deposition current.

After deposition, the samples were dipped in DI water in order to remove any excess solution, followed by annealing at 550°C for either 30 minutes, 3 hours or 5 hours to convert into hematite phase. The substrate post deposition, followed by annealing shows a visible orange colour, shown in Figure S2B. The range of voltages used was significantly higher than found in literature due to the low concentration $FeCl_3$ solution required to protect the YZnO.[39] The deposition process is summarised in Figure 2.

2.3 Structural and Physical Characterization

Scanning electron microscopy (SEM, Leica Stereoscan 420) was used to characterise the morphology of the ZnO NRs and their various coatings, INCA software (Oxford Instruments)

was used to measure the EDX spectra of the samples. To view the heterojunctions on a nanometre scale, a transmission electron microscope (TEM, JEOL, JEM1400-Plus, at 100kV)

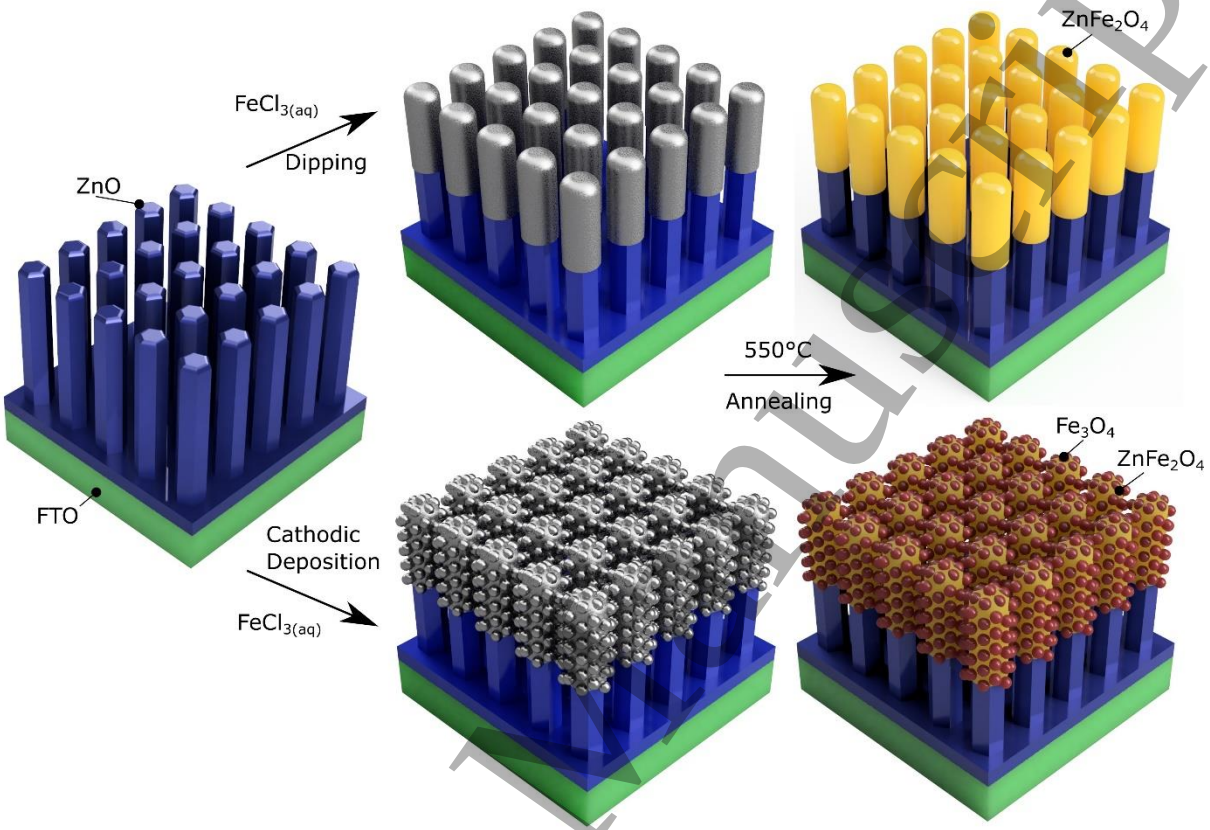

Figure 2: The proposed mechanism of electrochemical deposition steps, including submersion in $FeCl_3$ solution, reducing current and thermal annealing in air.

was used, as well as a high resolution TEM (HRTEM, JEOL-3010 at 300 kV). Microscopy images were processed using Image J software (National Institutes of Health, USA). And finally, available crystal phases on the sample were identified using powder x-ray diffraction (XRD, Siemens D500).

2.4 Photoelectrochemical and Optoelectronic Measurement

For the band gap energy measurement, a UV-Vis absorption spectroscopy was used (Lambda 265, PerkinElmer). Photoluminescence (PL) spectroscopy, used to infer recombination rate, was performed with a fluorescence spectrometer (PerkinElmer LS 45). Electrical Impedance Spectroscopy (EIS) was performed using a three electrode setup, with applied bias across the working photoanode and platinum counter electrode, and a KCl saturated Ag/AgCl reference electrode in a 1 M KOH aqueous electrolyte (pH 13.6). Nyquist plots were measured under illumination at a fixed DC potential (1 V_{RHE}) with a 10 mV AC sinusoidal modulation, at frequencies from 0.1 to 10,000 Hz. A calibrated solar simulator (Oriel LCS-100, Newport) including a built-in AM 1.5G filter with output power of 100 mW cm^{-2} was used as the light source. The electrochemical controller used for EIS measurement was Palm Sens 3 (Palm Sens BV) and the results were processed in PSTrace 4.5 (Palm Sens BV). The same system under dark conditions was used to measure Mott-Schottky plots at a fixed AC frequency of 1000 Hz, with a DC potential varied from 0 to 1.6 V vs RHE. Surface valence band measurements were performed using x-ray photoelectron spectroscopy (XPS, Thermo Scientific K-alpha using Al Kα source). PEC water splitting was tested using linear sweep voltammetry (LSV). Standard three electrode set up was used with a potentiostat (EA163, eDAQ) scanning in a range from 0 to 1.8 V_{RHE}. Incident photon to current conversion efficiency (IPCE) was measured at 1.23 V_{RHE} with a 300 W xenon lamp coupled with a monochromator. The incident light power was calibrated with a Newport optical power meter and silicon photodiode detector.

3 Results and Discussion

3.1 Structural and Physical Properties

When a cathodic current is applied, Fe^{3+}(aq) is reduced and deposited at the surface of the ZnO. The substrate changes colour from milky YZnO to a slight yellow tint with a dark grey

tone, shown in Figure S2B. Once the sample is annealed at 550°C, the Fe deposition is oxidised to α-Fe_2O_3 and the sample colour became more typical light brown.

The morphology of the hematite coated TCO YZnO array was studied by SEM, with a cross sectional image in Figure 3A and top down images in Figure S3. The hexagonal wurtzite ZnO NRs cross section is still visible after deposition at a low current density of 20 μA cm^{-2}, shown in Figure S3A. The light deposition, confirmed to be surface Fe_2O_3 by EDX (Figure S4), was also observed on the surface. The density of the Fe_2O_3 coating was increased with greater deposition current density. At 80 μA cm^{-2}, Figure S3C, the nanorod structure is overwhelmed, and the channels between the YZnO are filled by cross linked Fe_2O_3, leading to suppression of surface area. At 120 μA/cm^2, Figure S3D, the surface is completely covered by a connected film of hematite. This film will restrict the infiltration of electrolyte within the NRs and have negative effects on the photocatalytic performance. Thus, it is important to avoid such films while achieving optimum film thickness of the hematite on the NRs. Under our experimental conditions, the optimal hematite morphology was observed at 40 μA/cm^2, shown in Figure S3B. Nanocrystals of α-Fe_2O_3 are formed which increase surface roughness, beneficial to Faradic charge transfer to the electrolyte. The coated YZnO NRs show some brightened edges which can be associated to the formation of $ZnFe_2O_4$ at the interface between YZnO and Fe_2O_3. The top view SEM image in Figure S3A reveals bright rings on the edge of YZnO NRs. The formation of $ZnFe_2O_4$ and its effect on morphology was previously observed by Xu *et al.*[40] The edge brightening is likely due to the ferrimagnetic properties of $ZnFe_2O_4$ affecting the incoming electron beam.[41] The depth of the coating the overall surface morphology is better viewed in the angled cross sectional SEM of the 40 μA cm^{-2} sample, Figure 3A. The aggregates

of α-Fe_2O_3 nanocrystals are visible toward the tips of the wires. The $ZnFe_2O_4$ is indicated by the bright sleeves coating the YZnO side walls, causing the wires to become thicker away from the base.

Powder XRD was used to confirm the presence of ZnO, $ZnFe_2O_4$ and α-Fe_2O_3 on the surface, Figure 3B. XRD of pure Fe_2O_3 film without ZnO is also displayed as reference. The peaks observed confirm the presence of hematite, α-Fe_2O_3, with dominant peaks occurring at 24.5, 33.4, 36.1, 40.2 and 49.9° corresponding to crystal planes (012), (104), (110), (113) and (024) respectively (ICDD 01-075-5065). On the Y doped ZnO samples, the strongest (104) peak is seen increased intensity with greater deposition current, from just a shoulder at 20 µA cm^{-2}, to an obvious broad peak for 120 µA cm^{-2}. This is the only peak visible from α-Fe_2O_3 on the coated ZnO NRs due to the relative thin film coating and significant peak overlap with the ZnO and FTO. Meanwhile, ZnO peaks are clearly visible, dominated by the diffraction from the (002) plane at 34.8°, typical for vertically aligned ZnO NRs. Finally, only appearing in samples with both iron and ZnO depositions, a small peak at 43.0° is visible, matching the $ZnFe_2O_4$ (400) peak (ICDD 22-1012). The peak is visible in all the coated samples, but is most intense for 20 µA cm^{-2}, likely due to the majority of deposited Fe reacts with Zn to form $ZnFe_2O_4$ with the least formation of α-Fe_2O_3.

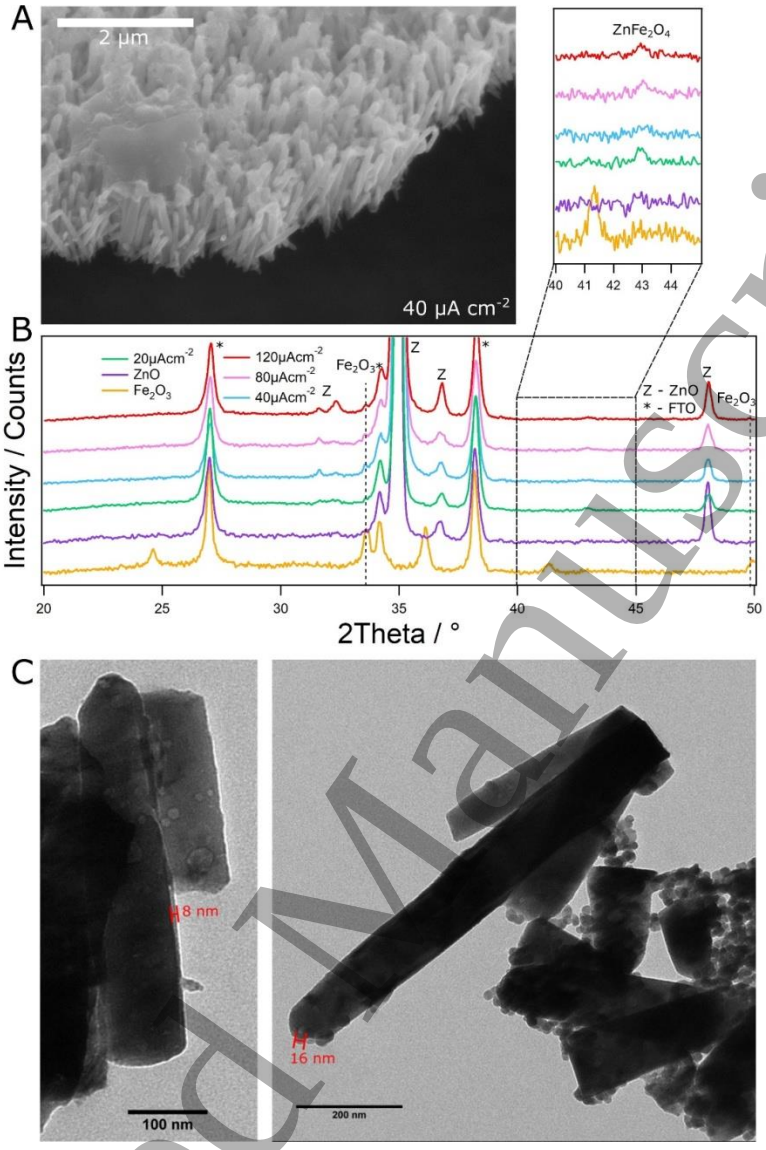

Figure 3: A. SEM image shows an angled cross sectional image of the 40 µA/cm^2 deposited sample after annealing. B. Powder XRD curves of various Fe_2O_3 coating thickness, along with pure ZnO and Fe_2O_3 samples, with expanded view of the $ZnFe_2O_4$ peak occurring at 43°C. TEM images of hematite coated ZnO NRs deposited at 40 µA/cm^2.

In order to accurately determine the structure of the triple junction at a nanometre scale, TEM was used to study the coated samples, shown in Figure 3C. A thin layer structure along with nanoparticles is observed coated on the NRs. The 8 nm thickness film directly attached to

the ZnO NRs is likely to be the $ZnFe_2O_4$. Such a thin layer explains the low intensity of the XRD peak. Connected nanoparticles forming a mesoporous network (right) are likely to associated with the α-Fe_2O_3 phase. The particles have an average diameter of 16 nm. This information sheds light on the advantages of electrochemical deposition, firstly there is a good electrical contact between the YZnO/$ZnFe_2O_4$ and YZnO/α-Fe_2O_3 interfaces, allowing smooth charge transfer. Secondly the iron phases with typically small minority carrier path length, have small enough domains that charge can reach the surface reaction centres before recombination.[42] Finally the nanoparticle network of α-Fe_2O_3 allows increased roughness and therefore surface area, than the smooth NRs, promoting high hole transfer rate to the electrolyte.

The structure of the triple junction was more clearly visible under HRTEM, as shown in Figure 4. In this case, atomic resolution was obtained for the NRs, nanoparticles and the thin film coating that encased the NRs. Such distinctive morphological features are clearly identified in the zoomed out view of Figure 4A, while Figure 4B, C and D respectively corresponds to their higher resolution images reviewing lattice constants of each phase. Unsurprisingly, the NR was confirmed as wurtzite zinc oxide with an atomic spacing of 2.45 Å, the (101) plane spacing, as well as displaying a (002) spot in the FFT of the image in Figure 4B. Figure 4C shows the atomic spacing of a spherical nanoparticle, showing high crystal orientation with 4.62 Å spacing, assigned as 2× (006) planar spacing of hematite. Finally, Figure 4C shows wide spacing of 4.88Å in the lighter region that forms the full coating around the NR. This is likely to be the 311 plane of $ZnFe_2O_4$ matching the dominant phase observed by Xu *et al.*[40]

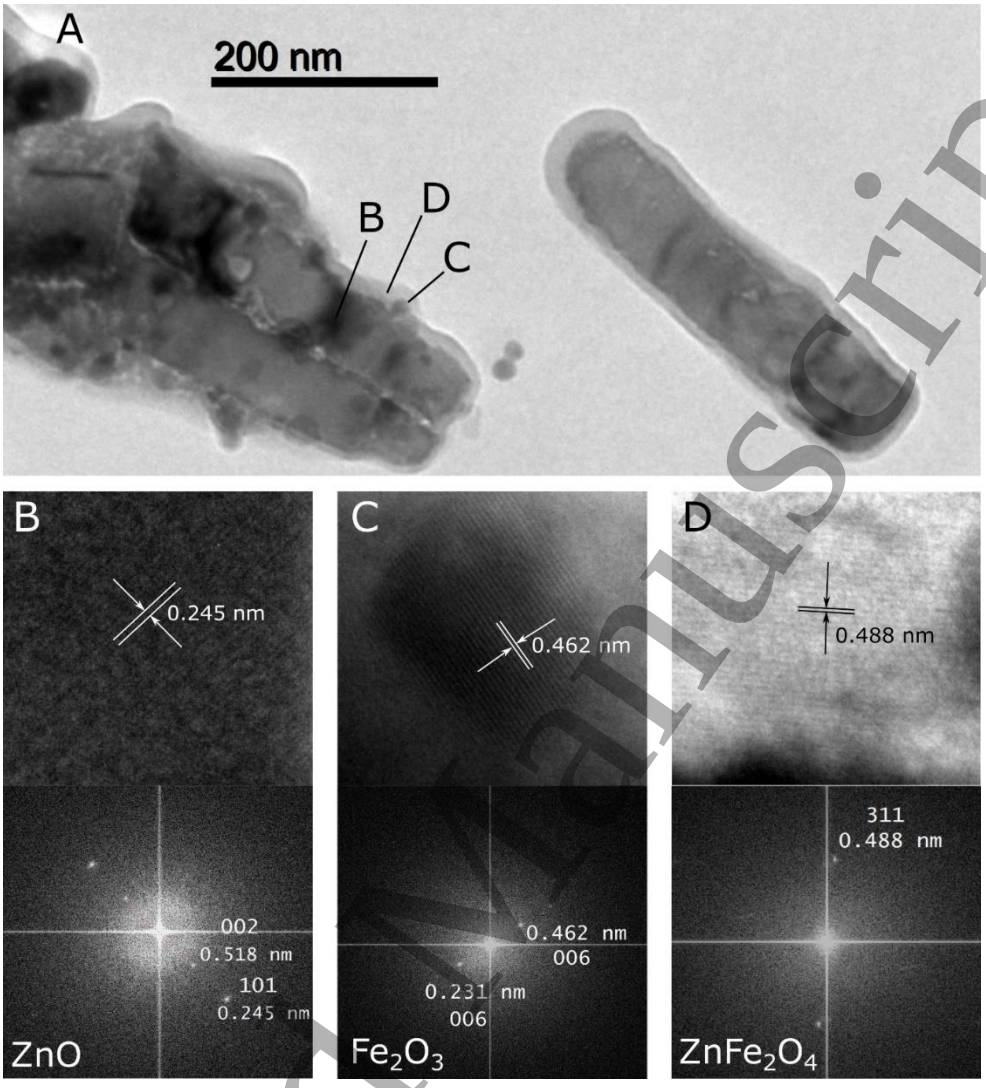

Figure 4: A. HRTEM micrograph of the sample at low magnification with specific sites labelled. B. The magnified image of the NR showing (top) atomic real space and (bottom) the FFT of the image. C. The nanoparticle magnified image with atomic spacing (top) and FFT (bottom). D. The thin film coating of the NR magnified, atomic spacing (top) and FFT (bottom).

In summary hematite nano crystals were formed together with a thin layer of $ZnFe_2O_4$ at the interface between YZnO and α-Fe_2O_3. This novel layered structure formed with three materials utilises the suitability of band edges allowing much improved charge separation and greatly increased visible sunlight water splitting. While highly conductive Y doped ZnO provides rapid

transport, α-Fe_2O_3 yields photoexcited electrons and $ZnFe_2O_4$ offers an effective electronic barrier blocking the return of electrons from ZnO to the α-Fe_2O_3.

3.2 Band Structure and Water Splitting Performance

With a composite layered semiconductor structure, an internal electrical field can be formed due to the alignment of their valance and conduction bands. This field could improve the charge separation and hence improve the photocatalytic charge efficiency. For PEC water splitting, they must form a junction with suitable band alignment to allow electron transfer away from the solution, and the converse for holes.[4]

To determine the band gap energies, E_g, of the junction, UV-Vis absorption measurements were applied to pure Fe_2O_3, YZnO and Fe_2O_3 coated YZnO samples (coated at 40 µA cm^{-2}). Tauc plots are shown in Figure 5A.[31] The UV-vis absorption spectra of all coated samples are displayed in the supplemental information in Figure S5A and B. Assuredly, the pure Fe_2O_3 sample and the YZnO yielded E_g values of 2.11 and 3.18 eV respectively, typical of these metal oxides. It is worth noting that the Y doped sample displayed a red shift compared to the pristine ZnO prepared by the same method, due to the doping forming new electronic states, outlined in greater detail in our previous work.[43] These results also show that the iron deposition has successfully sensitised the YZnO to visible light, allowing the generation of photoexcited electrons using a far greater portion of the solar spectrum. Electronic transitions from both ZnO and hematite are visible for the α-Fe_2O_3 coated YZnO NRs, but significantly shifted. The 2.11 eV gap associated with α-Fe_2O_3 gained a blue shift to 2.34 eV, and the YZnO experienced a red shift to 3.05 eV. This is likely due to two simultaneous doping effects caused by mobile zinc and iron ion migration from sustained 550°C heating. Firstly, Fe^{3+} introduced into the zinc oxide lattice has been previously shown to decrease the electronic band gap.[44] Secondly, Zn^{2+} is a

known p-type dopant for hematite,[45] this could impart new impurity states below the Fe_2O_3 valence band causing the blue shift. Finally, no discernible band gap could be determined for $ZnFe_2O_4$ therefore the value was taken from literature as 2.1 eV.[46]

In order to determine electronic properties, electrochemical impedance spectroscopy was used to determine key parameters. The electronic band configuration can be determined using the Mott-Schottky relation applied to EIS data taken in dark conditions, displayed in Figure 5B. Measurements were taken at a fixed frequency of 1 kHz and a voltage scanned from -0.4 to 1.6 V_{RHE} at 0.05 V intervals. The capacitance is modelled with a simple Randle's circuit, and the results are plotted $1/C^2$ against potential vs RHE. These plots in Figure 5B provide useful physical information such as dopant density N_D, and flat band potential, V_{FB}, corresponding to the Fermi level of the material. The M-S plot of pristine ZnO can be found in Figure S5C.

The determined M-S values can be found in Table S1 alongside their detailed calculation in the supporting information. Y doping leads to a significant increase in dopant density and a 0.2 V negative shift in V_{FB}, confirming the conductivity increase from doping. The carrier density of ZnO is nearly doubled with Y doping from 7.5×10^{25} m^{-3} (ZnO) to 1.35×10^{26} m^{-3} (YZnO), in agreement with our previous work.[37] This confirms the electron highway function of the conductive YZnO NRs which can efficiently transport charge to the FTO. The pure α-Fe_2O_3, conversely has a more positive value of V_{FB} alongside a lower n-type doping of 5.08×10^{25} m^{-3}.

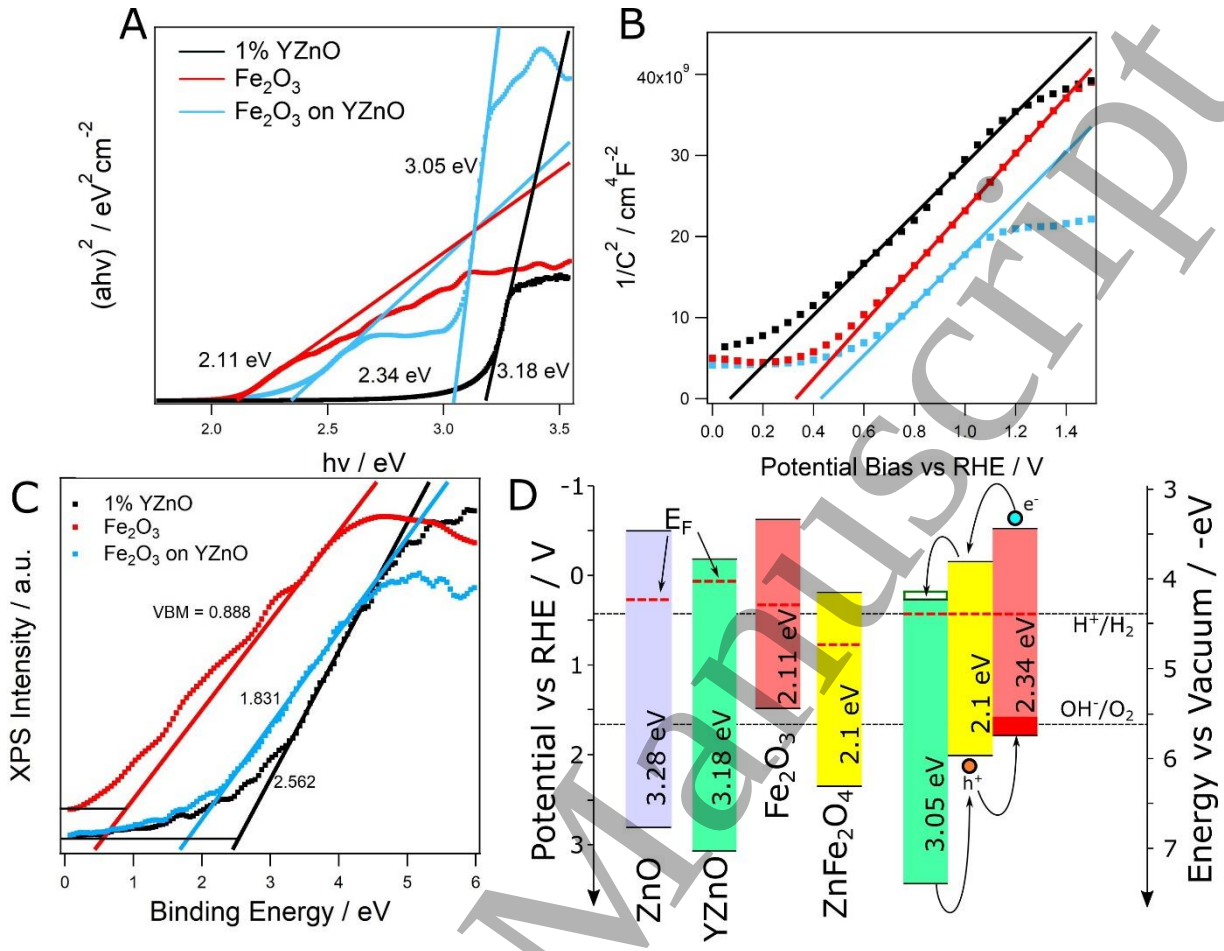

Figure 5: A shows the Tauc plots calculated from UV-Vis absorbance data used to calculate the direct band gaps of the samples. Mott-Schottky plots of the uncoated Y doped sample, the pure Fe_2O_3 sample and the optimised 40 µA coated sample are displayed in B. C shows the XPS valence band maxima survey of the samples. The calculated Fermi level, conduction band and valence band positions of the semiconductors found in this study are shown with respect to the redox potentials of water in D.

As no pure $ZnFe_2O_4$ sample was synthesised in this work, the precise band positions could not be determined. However, it was reported to have a V_{FB} of 0.83 V_{RHE} with an accompanying N_D value of 3.63 $\times 10^{22}$ m^{-3}.[47] These values are crucial as they determine the nature of the n-n junction. At the interface, the higher n-type doped sample will donate electrons forming a space charge region, equalising E_F across the junction.[48] Therefore, in this case,

YZnO will donate electrons to the contacting layer of $ZnFe_2O_4$ causing a positive potential shift in E_F in the former, and negative in the latter. By extension, the same effect will occur from Fe_2O_3 to $ZnFe_2O_4$, shifting E_F to be more positive within hematite.

XPS was also used to determine valence band (VB) position by scanning for the valence edge from 0 to 10 eV binding energy, followed by extrapolating linear regions to the base line intercept. Once the VB is determined, the conduction band edge was calculated using the corresponding E_g. The results for YZnO, Fe_2O_3 and the composite material can be found in Figure 5C, whereas the VB of undoped ZnO sample is displayed in Figure S5D. The VB of ZnO and YZnO were measured to be 2.182 and 2.562 eV respectively, in good agreement with literature.[17] The value for pristine Fe_2O_3 was determined to be more positive, at 0.888 eV, similar to the value of 1.4 eV determined by Li *et al.*[49] Finally the hematite coated YZnO NRs yielded a value of 1.831 eV. As a technique XPS is only surface sensitive, as the path length of electrons excited within the bulk is typically around a few nm due to rapid reabsorption.[50] Therefore, based on the HRTEM micrographs indicating homogenous coverage of $ZnFe_2O_4$, it can be assumed that the junction valence band maximum is due to this material, bolstered by its close match with previously reported values.[51] Using this information, the full electronic structure of the triple heterojunction can be mapped out, displayed in Figure 5D. By aligning the Fermi levels, it becomes clear that the triple junction has significant improved charge separation, which could enhance the efficiency for solar water splitting. Firstly, due to their significantly difference in E_g values, both UV and visible light will be utilised to generate holes. Secondly, the VB positions of the triple junction gives suitable alignment for rapid hole transfer from the core YZnO NRs through the $ZnFe_2O_4$ thin film to the surface particulate Fe_2O_3. Thirdly, the conduction band positions allow the electrons to cascade into the YZnO cores, which, in turn, shuttle electrons quickly to the counter electrode with high conductivity. This is essential for removing charge before recombination with holes and consequentially enable high

rate evolution of hydrogen at the platinum surface. This mechanism is confirmed by E_F/band shifts predicted by dopant density values, anticipating high performance solar water splitting.

The impact of the designed novel NR structure can be seen clearly in the dramatic enhancement in PEC water splitting, Figure 6. Firstly, the effects of Fe_2O_3 coating and the Y-doping in ZnO are presented in Figure 6A. With the 40 µA cm^{-2} Fe deposition rate, the photocurrent increased by 44% over the uncoated, undoped ZnO, from 0.66 to 0.83 mA/cm^2 at 1.23 V_{RHE}. This is due to the benefits of the n-n triple junction previously described, alongside the absorption of visible light photons due to the low band gap of Fe_2O_3 and $ZnFe_2O_4$. Using the additional beneficial transport properties of Y doping alongside coating, the performance increases further to 0.95 mA/cm^2. Despite high natural donor defect density in the microwave synthesised sample,[36] the conductivity gains by yttrium doping allow the same 40 µA cm^{-2} coating to yield 14% higher photocurrent at 1.23 V_{RHE}.[37] This is due to more efficient transportation of charge carriers from the solid/electrolyte interface by YZnO. The pure Fe_2O_3 sample shows critically low water splitting due to the high recombination and likely higher charge transfer resistance R_{CT}, managing 13 µA cm^{-2} at 1.23 V_{RHE}.

The performance is highly sensitive to the deposition current density as shown in Figure 6B, with the lightest coating, 20 µA cm^{-2}, only slightly outperforming the uncoated YZnO NRs. This is due to the lack of extra light absorption with such a thin layer of Fe_2O_3. Conversely the 120 µA cm^{-2} sample sees a large performance drop, achieving a lower photocurrent than the uncoated sample. The reasons for this are twofold, firstly the unfavourable morphology measured by SEM indicates a loss in surface area, restricting the access to electrolyte. Secondly, electron-hole recombination stifles the performance of thick Fe_2O_3 film, due to the short minority carrier path length in α-Fe_2O_3.[42] This is evidenced by the largest charge transfer resistance, R_{CT}, indicated by the greatest arc radius in its Nyquist plot, Figure S6A and B. The values of R_{CT} were calculated using a simple Randle's circuit and plotted against deposition

current in Figure S6C. A large R_{CT} is due to a greater resistive barrier for charge to overcome to enter the electrolyte, caused by the poor charge transportation of Fe_2O_3. The photoluminescence spectra in Figure S6D, directly measure the outgoing photons when recombination occurs. Once the photoabsorbing layer becomes sufficiently thick, the photoexcited electrons are unable to reach the YZnO resulting in increased charge recombination. Therefore an increase in PL intensity is seen with deposition current.

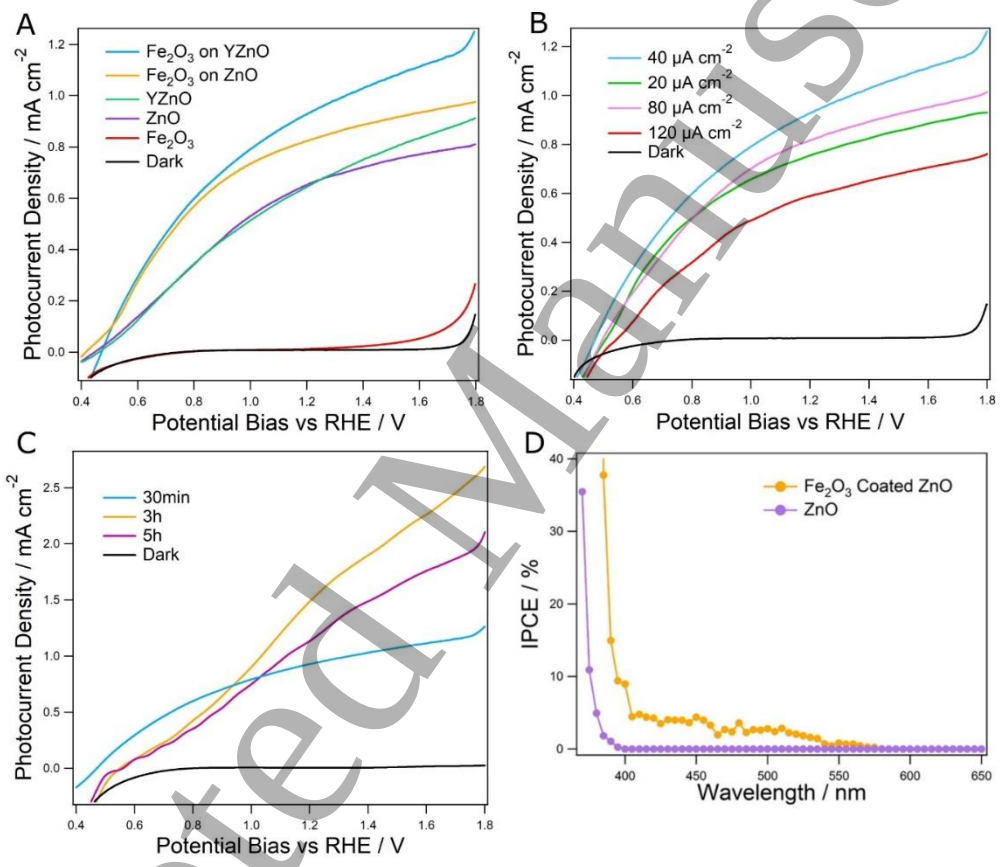

Figure 6: A shows the general comparison of doped vs undoped samples, with and without coating, the performance optimisation from the various electrodeposition currents is shown in B. C Shows the annealing duration optimisation, showing further enhancement, and finally D shows the incident photon to current efficiency.

The 40 μA cm^{-2} samples were further optimised by different durations of annealing. Longer periods of air annealing can be used to greatly improve the crystal quality of hematite,[33] reducing the electron hole recombination rates. The results are displayed in Figure 6C, displaying a dramatic further enhancement in photocurrent density for the optimised duration of 3 hours at 550°C, up to 1.59 mA cm^{-2} at 1.23 V_{RHE}. This 67% enhancement over the sample annealed for 30 minutes represents a significant improvement, and a 2.4 times increase over the uncoated nanorods. Stepped light/dark LSV was also performed, Figure S7A and B, which shows negligible dark currents. Furthermore, the optimised anode performances were stable in solution at a fixed potential of 1.23 V_{RHE}, shown in Figure S7C. There is no significant decay of photocurrent over time.

The optimised performance catapults this work to the frontier of solar water splitting, achieving nearly the highest photocurrent ZnO/iron oxide photoanode in literature. To the authors knowledge this is the most efficient solar water splitting device utilising a ZnO/Fe_2O_3 junction at 1.23 V_{RHE}. Typically these devices achieve negligible photocurrent in this potential region, requiring larger potential bias to promote water oxidation.[52–54] The most successful device constructed by Hsu *et al.* generated 1.25 mA cm^{-2} at 1.23 V_{RHE} through spin coating Fe_2O_3 on pristine ZnO NRs.[18] More success has been achieved by the coating of $ZnFe_2O_4$ on ZnO surfaces, with typical photocurrents ranging from 0.05 to 0.57 mA cm^{-2}.[55,56] The great achievement of 1.72 mA cm^{-2} by Xu *et al.* was achieved through coating Al doped ZnO, on NRs.[40] This implies further optimising the ZnO NRs with doping may improve our samples further.

Finally, incident photon to current conversion efficiency can be found in Figure 6D elegantly displaying the visible light sensitisation of the final sample. This data shows a significant efficiency increase at photon energies higher than 529 nm (2.34 eV) due to the Fe_2O_3 absorption onset, increasing to ~5% at 450 nm. Optical power density vs wavelength is

displayed in Figure S8. Some photocurrent is generated at wavelengths as long as 575 nm, likely due to the presence of the 8 nm layer of $ZnFe_2O_4$ on the rods, injecting electrons at even lower energies. This is in contrast to the uncoated ZnO sample which remained flat at wavelengths longer than 400 nm. At this wavelength the coated sample experiences a stark increase in efficiency again, due to the effective band gap reduction of ZnO, rising to 10% at 395 nm. All this confirms the success of the triple junction, able to absorb visible light photons and transfer photoexcited electrons to yttrium doped ZnO highways, for greatly improved solar water splitting.

4 Conclusion

In conclusion a novel electrodeposition method was developed and used to build a $ZnO/Fe_2O_3/ZnFe_2O_4$ triple junction photoanode, based on yttrium doped ZnO NRs. The new coating method allowed fine control the morphology of hematite grown on the surface of the nanorods, as evidenced by SEM, XRD and TEM. Meanwhile the presence of $ZnFe_2O_4$ was also confirmed, forming a thin layer coating on the NRs. This had the effect of sensitising the ZnO to visible light, as evidenced through UV-Vis absorption spectroscopy and IPCE, utilising a favourable junction cascade for electron transfer to the ZnO and hole transfer to the solution. This effectively reduced the charge recombination effects in α-Fe_2O_3 as measured by EIS and PL spectroscopy, leading to an optimised coating thickness at a current density of 40 μA cm^{-2}. The yttrium doping of the NRs yielded a 14% enhancement over the pristine ZnO NRs, confirming the effects of conductive ZnO in addition to its photon trapping and light waveguiding effects. Optimising hematite crystallinity by control the annealing process led to a champion photocurrent of 1.59 mA cm^{-2} at 1.23 V_{RHE}, representing a 2.4 times enhancement over the uncoated ZnO NRs. This work represents an important advancement in the application of nanostructured junctions to PEC water splitting.

Supporting information

Electronic Supplementary Information (ESI) available: Contains reflectance calculation, electrodeposition schematic, sample photographs, current time deposition profile, top down SEM, EDX mapping, band position calculation with table of electronic parameters, UV-Vis absorption spectra, MS plot of pristine ZnO with XPS valence band survey, Nyquist plots of the samples R_{CT} plotted against deposition current, PL spectra, on/off illuminated LSVs, chronoamperometry, current decay and the optical power density spectrum of the xenon lamp used for IPCE.

Author Information

Corresponding Author:

*dancommandeur@gmail.com

ORCID

Daniel Commandeur: 0000-0002-7179-2370

Qiao Chen : 0000-0001-5424-4818

The authors declare no competing financial interest.

Acknowledgements

The authors would like to thank the University of Sussex school of life sciences for funding. The authors would also like to thank Professor Jawwad Darr for his support on this project at University College London.

References

[1] F. Creutzig, B. Fernandez, H. Haberl, R. Khosla, Y. Mulugetta, K. C. Seto, *Annu. Rev. Environ. Resour.* **2016**, *41*, 173–198.

[2] R. J. Millar, J. S. Fuglestvedt, P. Friedlingstein, J. Rogelj, M. J. Grubb, H. D. Matthews, R. B. Skeie, P. M. Forster, D. J. Frame, M. R. Allen, *Nat. Geosci.* **2017**, *10*, 741–747.

[3] A. Fujishima, K. Honda, *Nature* **1972**, *238*, 37–38.

[4] D. G. Nocera, *Acc. Chem. Res.* **2012**, *45*, 767–76.

[5] M. G. Walter, E. L. Warren, J. R. McKone, S. W. Boettcher, Q. Mi, E. A. Santori, N. S. Lewis, *Chem. Rev.* **2010**, *110*, 6446–6473.

[6] L. Kavan, M. Grätzel, *Electrochim. Acta* **1995**, *40*, 643–652.

[7] M. Wang, F. Ren, J. Zhou, G. Cai, L. Cai, Y. Hu, D. Wang, Y. Liu, L. Guo, S. Shen, *Sci. Rep.* **2015**, *5*, 12925.

[8] C. F. Tan, A. K. Su Su Zin, Z. Chen, C. H. Liow, H. T. Phan, H. R. Tan, Q.-H. Xu, G. W. Ho, *ACS Nano* **2018**, *12*, 4512–4520.

[9] C. F. Tan, W. L. Ong, G. W. Ho, *ACS Nano* **2015**, *9*, 7661–7670.

[10] A. Janotti, C. G. Van de Walle, *Reports Prog. Phys.* **2009**, *72*, 126501.

[11] N. M. Vuong, J. L. Reynolds, E. Conte, Y. I. Lee, *J. Phys. Chem. C* **2015**, *119*, 24323–24331.

[12] W. Zhen, X. Ning, B. Yang, Y. Wu, Z. Li, G. Lu, *Appl. Catal. B Environ.* **2018**, *221*, 243–257.

[13] U. Gupta, C. N. R. Rao, *Nano Energy* **2017**, *41*, 49–65.

[14] Y. Fang, W. C. Lee, G. E. Canciani, T. C. Draper, Z. F. Al-Bawi, J. S. Bedi, C. C. Perry, Q. Chen, *Mater. Sci. Eng. B* **2015**, *202*, 39–45.

[15] K. Maeda, K. Domen, *J. Phys. Chem. C* **2007**, *111*, 7851–7861.

[16] H. S. Han, S. Shin, D. H. Kim, I. J. Park, J. S. Kim, P. S. Huang, J. K. Lee, I. S. Cho, X. Zheng, *Energy Environ. Sci.* **2018**, *11*, 1299–1306.

[17] Y. Fang, Y. Xu, X. Li, Y. Ma, X. Wang, *Angew. Chemie Int. Ed.* **2018**, *57*, 9749–9753.

[18] Y. K. Hsu, Y. C. Chen, Y. G. Lin, *ACS Appl. Mater. Interfaces* **2015**, *7*, 14157–14162.

[19] R. F. G. Gardner, R. L. Moss, D. W. Tanner, *Br. J. Appl. Phys.* **1966**, *17*, 55–61.

[20] B. Warnes, F. Aplan, G. Simkovich, *Solid State Ionics* **1984**, *12*, 271–276.

[21] N. A. Jayah, H. Yahaya, M. R. Mahmood, T. Terasako, K. Yasui, A. M. Hashim, *Nanoscale Res. Lett.* **2015**, *10*, 1–10.

[22] K. Sivula, F. Le Formal, M. Grätzel, *ChemSusChem* **2011**, *4*, 432–49.

[23] S. R. Pendlebury, X. Wang, F. Le Formal, M. Cornuz, A. Kafizas, S. D. Tilley, M. Grätzel, J. R. Durrant, *J. Am. Chem. Soc.* **2014**, *136*, 9854–9857.

[24] A. G. Joly, J. R. Williams, S. A. Chambers, G. Xiong, W. P. Hess, D. M. Laman, *J. Appl. Phys.* **2006**, *99*, 053521.

[25] Y. Lin, G. Yuan, S. Sheehan, S. Zhou, D. Wang, *Energy Environ. Sci.* **2011**, *4*, 4862.

[26] T. W. Hamann, *Dalt. Trans.* **2012**, *41*, 7830.

[27] A. Kay, I. Cesar, M. Grätzel, *J. Am. Chem. Soc.* **2006**, *128*, 15714–15721.

[28] Y. Hou, C. Zheng, Z. Zhu, X. Wang, *Chem. Commun.* **2016**, *52*, 6888–6891.

[29] A. Subramanian, A. Annamalai, H. H. Lee, S. H. Choi, J. Ryu, J. H. Park, J. S. Jang, *ACS Appl. Mater. Interfaces* **2016**, *8*, 19428–19437.

[30] M. T. Mayer, C. Du, D. Wang, *J. Am. Chem. Soc.* **2012**, *134*, 12406–12409.

[31] D. K. Zhong, M. Cornuz, K. Sivula, M. Grätzel, D. R. Gamelin, *Energy Environ. Sci.* **2011**, *4*, 1759.

[32] K. Y. Yoon, H. J. Ahn, M. J. Kwak, S. I. Kim, J. Park, J. H. Jang, *J. Mater. Chem. A* **2016**, *4*, 18730–18736.

[33] H.-J. Ahn, M.-J. Kwak, J.-S. Lee, K.-Y. Yoon, J.-H. Jang, *J. Mater. Chem. A* **2014**, *2*, 19999–20003.

[34] X. Wang, K. Q. Peng, Y. Hu, F. Q. Zhang, B. Hu, L. Li, M. Wang, X. M. Meng, S. T. Lee, *Nano Lett.* **2014**, *14*, 18–23.

[35] H. Gao, C. Liu, H. E. Jeong, P. Yang, *ACS Nano* **2012**, *6*, 234–240.

[36] D. Commandeur, G. Brown, E. Hills, J. Spencer, Q. Chen, *ACS Appl. Nano Mater.* **2019**, *2*, 1570–1578.

[37] D. Commandeur, G. Brown, P. McNulty, C. Dadswell, J. Spencer, Q. Chen, *J. Phys. Chem. C* **2019**, *123*, 18187–18197.

[38] W. C. Lee, Y. Fang, R. Kler, G. E. Canciani, T. C. Draper, Z. T. Y. Al-Abdullah, S. M. Alfadul, C. C. Perry, H. He, Q. Chen, *Mater. Chem. Phys.* **2015**, *149–150*, 12–16.

[39] S. Peulon, H. Antony, L. Legrand, A. Chausse, *Electrochim. Acta* **2004**, *49*, 2891–2899.

[40] Y. F. Xu, H. S. Rao, X. D. Wang, H. Y. Chen, D. Bin Kuang, C. Su, *J. Mater. Chem. A* **2016**, *4*, 5124–5129.

[41] M. Lorenz, M. Brandt, K. Mexner, K. Brachwitz, M. Ziese, P. Esquinazi, H. Hochmuth, M. Grundmann, *Phys. status solidi - Rapid Res. Lett.* **2011**, *5*, 438–440.

[42] L. Zhang, L. Sun, Z. Guan, S. Lee, Y. Li, H. D. Deng, Y. Li, N. L. Ahlborg, M. Boloor, N. A. Melosh, et al., *Nano Lett.* **2017**, *17*, 5264–5272.

[43] H. A. Rakhshani, A. E.; Makdisi, Y.; Ramazaniyan, *J. Appl. Phys.* **1998**, *83*, 1049.

[44] T. Srinivasulu, K. Saritha, K. T. R. Reddy, *Mod. Electron. Mater.* **2017**, *3*, 76–85.

[45] Y. C. Chen, C. L. Kuo, Y. K. Hsu, *J. Alloys Compd.* **2018**, *768*, 810–816.

[46] X.-L. Zheng, C.-T. Dinh, F. P. G. de Arquer, B. Zhang, M. Liu, O. Voznyy, Y.-Y. Li, G. Knight, S. Hoogland, Z.-H. Lu, et al., *Small* **2016**, *12*, 3181–3188.

[47] N. Helaili, G. Mitran, I. Popescu, K. Bachari, I. C. Marcu, A. Boudjemaa, *J. Electroanal. Chem.* **2015**, *742*, 47–53.

[48] S. S. Kalanur, I. H. Yoo, J. Park, H. Seo, *J. Mater. Chem. A* **2016**, *5*, 1455–1461.

[49] J. Li, F. Meng, S. Suri, W. Ding, F. Huang, N. Wu, *Chem. Commun.* **2012**, *48*, 8213–8215.

[50] I. Doron-Mor, A. Hatzor, A. Vaskevich, T. Van Der Boom-Moav, A. Shanzer, I. Rubinstein, H. Cohen, *Nature* **2000**, *406*, 382–385.

[51] X. L. Zheng, C. T. Dinh, F. P. G. de Arquer, B. Zhang, M. Liu, O. Voznyy, Y. Y. Li, G. Knight, S. Hoogland, Z. H. Lu, et al., *Small* **2016**, *12*, 3181–3188.

[52] C. Zhang, W. Fan, H. Bai, X. Yu, C. Chen, R. Zhang, W. Shi, *ChemElectroChem* **2014**, *1*, 2089–2097.

[53] A. Ikram, S. Sahai, S. Rai, S. Dass, R. Shrivastav, V. R. Satsangi, *Int. J. Hydrogen Energy* **2015**, *40*, 5583–5592.

[54] M. Chakraborty, D. Roy, A. Biswas, R. Thangavel, G. Udayabhanu, *RSC Adv.* **2016**, *6*, 75063–75072.

[55] D. D. Qin, C. L. Tao, *RSC Adv.* **2014**, *4*, 16968.

[56] A. Sheikh, A. Yengantiwar, M. Deo, S. Kelkar, S. Ogale, *Small* **2013**, *9*, 2091–2096.